

GRAVITATIONAL FRAGMENTATION: A COMPARISON WITH W49A

ERIC R. KETO,^{1,2,3} JOHN C. LATTANZIO,^{4,5} AND JOE J. MONAGHAN⁴*Received 1990 December 12; accepted 1991 June 19*

ABSTRACT

We investigate the process of gravitational fragmentation of molecular clouds through a comparison of numerical and observational results. We calculate the expected millimeter wave molecular line emission from a model fragmenting cloud generated by a numerical hydrodynamic simulation and compare with observations of HCO⁺ from the star-forming region W49A. Our investigation suggests that the rotating ring of H II regions, the necklace in W49A, may have formed in the gravitational fragmentation of a flattened rotating molecular cloud.

Subject headings: hydrodynamics — interstellar: molecules — nebulae: H II regions — nebulae: individual (W49) — stars: formation

1. INTRODUCTION

Previous studies indicate that gravitational fragmentation will occur in flattened or filamentary structures, but that fragmentation during three-dimensional free-fall is a highly inefficient process if, in fact, it can occur at all (Layzer 1963; Hunter 1964; Goldreich & Lynden-Bell 1965a, b; Larson 1972, 1985; Tohline 1980a, b; Gingold & Monaghan 1983; Rozyczka 1983; Monaghan & Lattanzio, hereafter ML). Thus, if clusters of massive stars form through gravitational fragmentation, then the fragmentation must necessarily occur in gas which is a sheet or filament. Following this line of reasoning, massive stars may form through fragmentation of a molecular cloud after an initial collapse along a preferred direction produces a flattened structure.

In this paper we continue the investigation of gravitational fragmentation begun in ML. We compare one of the hydrodynamic models of ML, a gas cloud flattened by rotation, with molecular line observations of massive star-forming regions. The comparison is effected through a numerical calculation of the observable molecular line radiation of the model fragmenting cloud. The model chosen was selected because of a resemblance to the W49A star-forming region. A comparison of the modeled and observed spectral line data suggests that the rotating ring of H II regions, the necklace in W49A, may be the result of fragmentation of a flattened, rotating molecular cloud.

In the following sections of this paper we briefly review those aspects of the hydrodynamical model which are relevant to this discussion, describe our new calculation of the observable spectral line emission, and compare our modeled spectra with previously published observations.

2. GRAVITATIONAL FRAGMENTATION

2.1. Numerical Hydrodynamics

We borrow the hydrodynamic calculations described in § 10.4 of ML. This calculation follows the collapse of a spherical cloud of total mass $M = 10^4 M_\odot$, with an initial radius $R = 12.6$ pc, temperature 70 K, and density 20 cm^{-3} . The initial ratio of thermal to gravitational energy, $\alpha = 5\mathcal{R}TR/3(\gamma - 1)GM\mu = 0.3$, where the adiabatic index, $\gamma = 1.4$, is appropriate for molecular gas at temperatures less than 80 K, $\mu = 2.33$ is the mean molecular weight, and \mathcal{R} is the gas constant. The cloud is set rotating with a constant Ω giving an equatorial velocity of 2.2 km s^{-1} . The ratio of rotational to gravitational energy, $\beta = \Omega^2 R^3/GM = 0.47$. Thus, in the absence of rotation, the cloud is unstable to gravitational collapse. With the rotation, we expect the collapse to proceed along the rotation axis, while, perpendicular to this axis, the rotation will support the cloud against collapse. The cloud has an average constant density but with a field of random perturbations with a standard deviation of 14%. The initial cooling, free-fall, and rotation time scales are about 1, 4, and 35 million years.

The initial collapse of the spherical cloud down the rotation axis produces a hydrodynamically self-consistent, rotating disk in average centrifugal force balance. The density distribution is centrally condensed and approximately that of a projected sphere, $n \propto [1 - (r/R)^2]^{1/2}$. This disk may be taken as a more realizable starting configuration for the fragmentation and could form from a variety of initial states including non-spherical, nonuniform clouds.

Initially the small perturbations grow slowly, and a noticeable asymmetry in the density is not seen until about two initial free-fall times after the calculation is started. Figure 1, adapted from ML, shows the particle positions projected onto the equatorial plane between 2.0 and 2.7 free-fall times of the initial configuration (because we used equal-mass particles this is proportional to the projected surface density). Once the fragments begin to separate out, the structure of the disk changes quickly. By ~ 2.5 (initial) free-fall times much of the disk is nearly cleared into a set of dense filaments and fragments, arranged roughly in a ring, as seen in the figure. Table 1 gives the masses, characteristic radii, and individual free-fall time scales, $t_{\text{ff}} = (4\pi G\rho_{\text{frag}})^{-1/2}$ of the labeled fragments. At this

¹ Postal address: Smithsonian Astrophysical Observatory, 60 Garden Street, Cambridge, MA 02138.

² Laboratory for Astronomical Imaging, University of Illinois, 1002 West Green Street, Urbana, IL 61801.

³ Participating Guest: Institute of Geophysics and Planetary Physics, Lawrence Livermore National Laboratory, L-413, P.O. Box 808, Livermore, CA 94550.

⁴ Postal address: Department of Mathematics, Monash University, Clayton, Victoria, 3168, Australia.

⁵ Also Department of Astronomy, University of California, Berkeley, CA 94720.

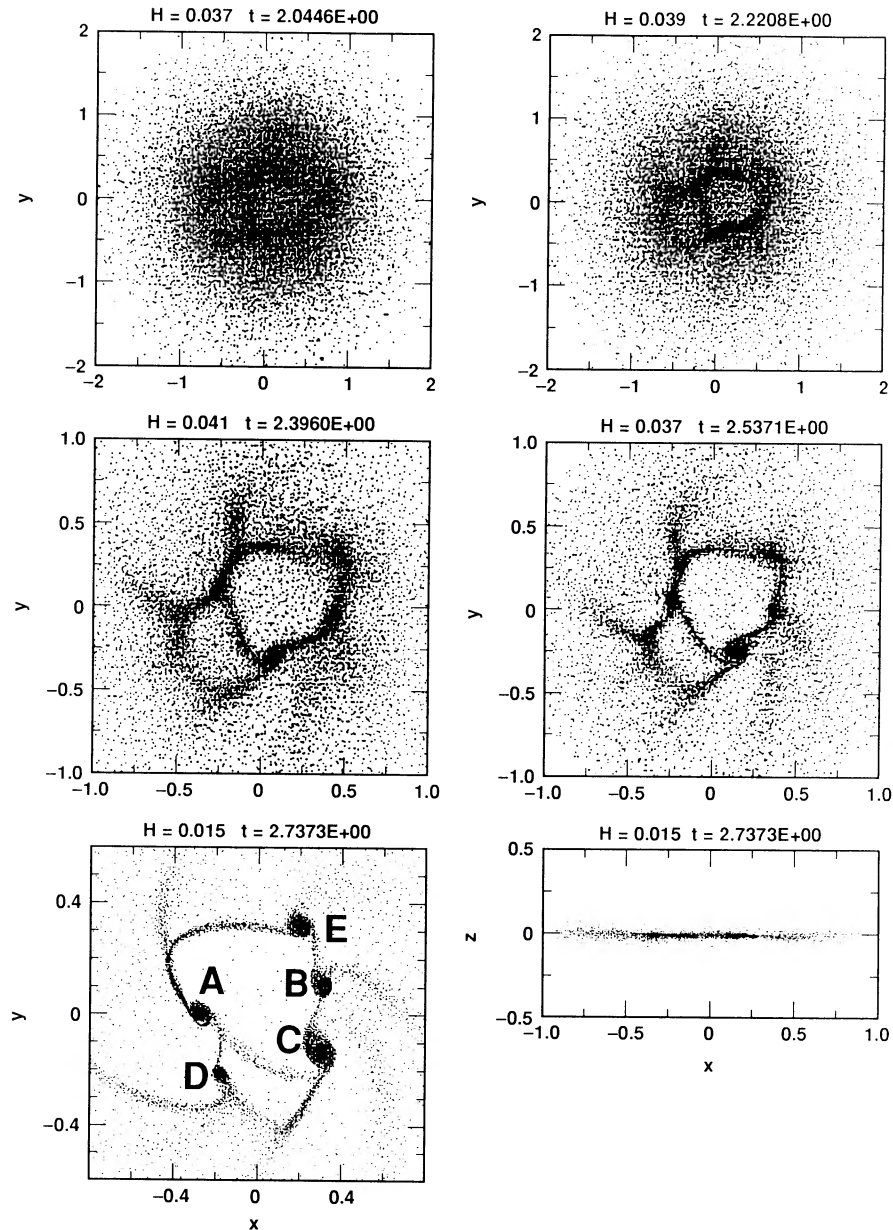


FIG. 1.—Particle positions in the x - y plane for the perturbed sphere described in the text. The length unit is 12.6 pc. The times are quoted in units of the initial free-fall time, and h is the resolution length. The last frame shows the thickness of the disk.

point, about half the total mass of the original cloud is contained in the cores, with the remainder in the lower density filaments which connect them, and in the disk. There are no fluid particles remaining in most of the volume of the original cloud.

TABLE 1
FRAGMENT SCALES OF THE NUMERICAL SIMULATION

Label	Mass (M_{\odot})	Radius (pc)	Free-Fall Time (10^5 yr)
A.....	1300	0.6	3.3
B.....	800	0.6	4.2
C.....	1400	0.8	4.9
D.....	500	0.4	2.9
E.....	700	0.6	4.5

The pattern of condensations seems more consistent with the growth of a grid of perturbations rather than the development and breakdown of a circularly symmetric ring. For example, in the structures shown in Figure 1, the largest void develops off center and the ring is never, even in the early stages, symmetric about the origin of the initial disk. Thus the pattern of condensations and voids in the disk may represent a tessellation of the disk surface, and the apparent ring structure a reflection of the boundary of the limited surface area of the disk.

Figure 2 shows the velocity field of the last computed model corresponding to the same evolutionary time as shown in the last frame of Figure 1. The significant dynamical structures in the model are the rotation of the fragmented ring of cores and the localized three-dimensional collapse of the individual cores

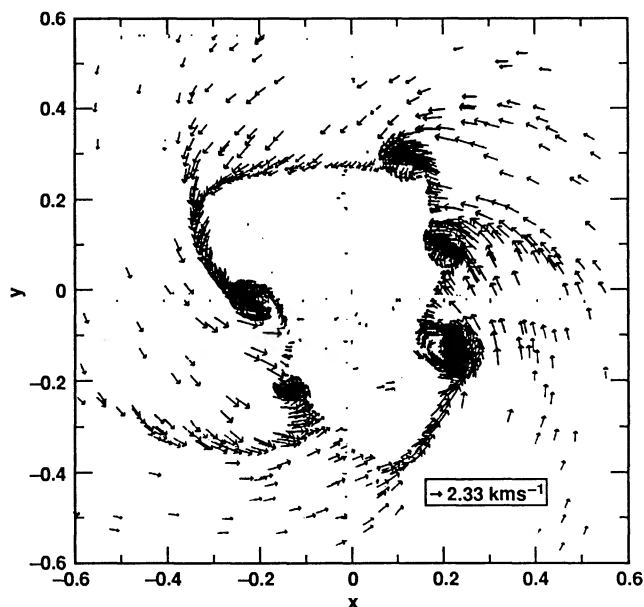


FIG. 2.—The velocity field in the equatorial plane for the last calculated model. The velocity unit is 1.85 km s^{-1} .

under their own self-gravity. Because of the angular momentum present in the original cloud, the collapse of the individual cores is manifest as an accretion flow involving both the rotation of the cores about their own axes (spin) and infall.

To check that this ringlike morphology was a result of the initial cloud structure and not a particular perturbation field, we ran six different realizations of the same model. Reassuringly, four of these formed well-defined “rings” of dense cores. In each case, the ring phase lasted only about one-half of the initial free-fall time of the cloud.

2.2. Analytic Idealization

We may compare the numerical results with the results predicted from stability analysis of an idealized cloud assuming a stationary, uniform initial state, infinite in extent. In the thin sheet approximation the maximum growth rate occurs at wave number

$$k_{\max} = \frac{1}{H} = \frac{\pi G \sigma}{c^2}$$

where H is the characteristic length scale and σ is the surface density. The effect of rotation on such an unbounded disk has been studied by Hunter (1972) and Goldreich & Lynden-Bell (1965) and acts only to slow the growth rate without altering the length scale. For the parameters of our numerical model, the growth rate is slowed by about a factor of 2.

For comparison we use the average properties of our non-uniform thermally evolving numerical model. Thus, for example, for the surface density of the sheet we use the total mass averaged over the initial area of the disk, $\sigma = M/\pi R^2$, and for the gas we use the temperature at approximately one dynamical time, or $\sim 20 \text{ K}$. In this case, the parameter α , defined earlier as the ratio of thermal to gravitational energy, will be ~ 0.1 . Using these approximations we would expect the characteristic size scale to be $\lambda_{\max} = \frac{4}{\pi} \pi \alpha R$ or $\lambda_{\max} = 0.2R$, which is close to the mean separation of $0.3R$ seen in Figure 1.

The time scale for the growth of fragments in the thin disk

approximation is 1 million years with $T = 20 \text{ K}$, scaling as $T^{1/2}$, or ~ 2 million years if allowing for the effects of rotation. This is in reasonable agreement with the evolutionary time calculated in the numerical simulation which is ~ 0.6 scaled units of time or 3.7 million years. (One initial free-fall time was required to form the disk from the sphere.) This is longer than we would expect for the lifetime of a star-forming region, based on the lifetimes of OB stars. However, the numerical simulation of ML begins with a number density of 20 cm^{-3} , much less than found in typical massive star-forming regions. In the next section we will suggest how the simulation may be scaled to more appropriate densities, about a factor of 1000 higher. The corresponding decrease in the relevant time scales is about a factor of 30, resulting in a characteristic time of 10^5 yr .

3. SPECTRAL CHARACTERISTICS

3.1. Synthetic Spectra

From the data provided by the numerical simulation of the fragmentation, we can calculate a synthetic observational data set using the radiative transfer code described in Keto (1990, and used in a similar fashion in Keto & Lattanzio 1989). For comparison with available observations we have chosen to model the emission of the commonly observed molecule $\text{HCO}^+(1 \rightarrow 0)$ at 89 GHz. For the present calculation, the level populations of HCO^+ are set locally in the optically thin approximation (Dickel & Auer 1991). In our model $[\text{HCO}^+]/[\text{H}_2] = 10^{-9}$.

To make an effective comparison we must include in our simulation the effect of the observed H II regions as sources of strong continuum radiation which heats the gas immediately around the cores and causes the foreground molecular gas to be seen in absorption, as in the actual observations. We have thus assumed that in each of the five cores in our model there is an H II region of diameter 0.1 pc, which would result from star formation in the modeled cores which would take place on a scale well below the resolution of the hydrodynamic simulation and involve physics not incorporated into the code. We take the temperature of the ionized gas to be 8000 K, and the optical depth at 89 GHz to be 0.003. The temperature of the molecular gas surrounding the H II regions is altered according to the prescription given by Scoville & Kwan (1979) for the UV heating of dust and gas surrounding an embedded source, namely:

$$T = 100 \text{ K} \left(\frac{r}{0.065 \text{ pc}} \right)^{-0.5}$$

For better comparison with the observations we have assumed that the model disk lies at an arbitrarily chosen viewing angle of 30° . Figure 3 shows the velocity integrated HCO^+ emission, and Figure 4 individual spectra at the positions of the cores. Both figures assume an observational resolution of $15''$.

3.2. Observed Spectra

3.2.1. Rotation of the Necklace

Figure 5, showing the V_{LSR} of our model H II regions, may be compared with the observations of the H76 α recombination lines of Welch et al. (1987). Both the observed and modeled velocities show a similar dispersion about a linear gradient across the ring, 18% and 17% of the respective ranges. In both the predicted and observed cases the dispersion indicates

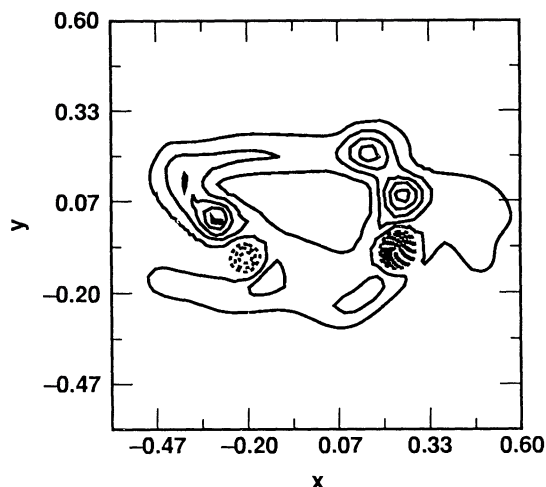


FIG. 3.—Velocity integrated HCO^+ emission. Dashed contours denote negative values. The contour interval is 0.2 K km s^{-1} .

departure from orbital symmetry. The calculation of ML produces a transitory ring phase, lasting for about one initial free-fall time. This description is, of course, a relative one: the average lifetime of the stars in W49A is only a few million years (Dreher et al. 1984).

The magnitude of the modeled line-of-sight velocity gradient due to rotation, 1.75 km s^{-1} per 6.3 pc is about a factor of 27 less than the gradient observed in W49A, 15 km s^{-1} per 2.0 pc . The difference relates primarily to the difference in mass density between the simulated and observed clouds. The initial density in the hydrodynamic simulation is $10^4 M_{\odot}$ in a 12.6 pc radius, or $8 \times 10^{-23} \text{ g cm}^{-3}$, about a factor of 1000 less than would be appropriate to replicate the conditions in W49A. We may improve the hydrodynamic simulation as a model for W49A by an approximate scaling. The hydrodynamics in the simulation scale around the two parameters, α and β , the ratios of thermal and rotational energies to the gravitational energy. Except for the differences imposed by the scale-dependent radiative cooling, the numerical simulation may represent any model cloud with the properties of mass, radius and temperature chosen so that $\alpha = 0.3$ and $\beta = 0.47$. If we were to choose a radial size of one-fourth the current model size and an angular velocity 27 times larger to match W49A, then if we adopted a mass 11.4 times the current mass, β would be the same. If we chose a temperature of 45 times the current model temperature, α would be the same. We would then have a model cloud of mass $1.1 \times 10^5 M_{\odot}$, radius 3.15 pc , density of $1.5 \times 10^4 \text{ cm}^{-3}$, and a rotational velocity of 15 km s^{-1} at the equatorial radius. A simulation of this model would result in a similar structure except for the differences imposed by the scale-dependent radiative cooling. The initial temperature is somewhat irrelevant to the calculation since the molecular cloud will cool rapidly on a time scale short compared to the dynamical time. The value of α after cooling to $\sim 10 \text{ K}$ will differ in the two calculations; however, this should not be important because the gravitational energy always dominates the thermal energy, especially with the cooling. Although the large rotational velocity in our scaled model is atypical of that observed in star-forming regions, the magnitude is motivated by the observed velocity gradient in W49A, which is unlike any other known star-forming region in the galaxy. We suggest that the rotating ring of star formation in W49A must result

from an unusually high angular momentum in the parent cloud at the time of initial collapse.

3.2.2. Accretion Flows of the Cores

Our synthetic spectra all show split lines as expected from the model velocity field (see Fig. 2). Because all our model H II regions have the same continuum radiation temperature, whether the individual lines are seen in emission or absorption depends on the optical depth and excitation temperature of the foreground molecular gas. In the cases where both lines are seen in emission the H II regions are located before the midplane of the flattened disk as seen by the observer. Where both lines are seen in absorption, the H II region is behind the midplane. For H II regions near the midplane the foreground gas is seen in absorption while the background gas is seen in emission. The resulting lines appear as an inverse P Cygni profile. This profile is seen in the W49A data of Welch et al. (1987), while split lines, both in emission and absorption, are seen in the W51 data of Rudolph et al. (1990).

The magnitude of the splitting in our model spectra is a factor of ~ 5 less than observed, and the modeled and observed brightnesses differ by about a factor of 15. This may relate to the lower density of the model of ML with respect to that inferred in W49A. In our scaled model the increased density will increase the splitting as $(GM/R)^{1/2}$, a factor of $(11/0.25)^{1/2}$ or 7 for the values quoted previously, and increase the line brightness by an amount proportional to the column density $N \propto M/R^2$.

Welch et al. suggest that where the split lines are seen in their data the splitting is consistently found at $\sim 15 \text{ km s}^{-1}$. We note that in the model the line splitting is consistently 3 km s^{-1} , or $\sim 21 \text{ km s}^{-1}$ when scaled. The similarity in the magnitude of the splitting relates to the similarity in the mass and size scales of the individual fragments in each of the two cases, modeled and observed. This is because within the cores the gravitationally bound velocities scale with the fragment mass and size, $v \propto (m_{\text{core}}/r_{\text{core}})^{1/2}$. The similarity in core scale is, as explained in § 2.2, intrinsic to the fragmentation process. We therefore suggest that the cores of W49A are themselves of similar scale.

While we may measure the similarity of mass, radius, and infall velocity in the hydrodynamic model (see § 3.1), and we may infer a similarity in infall velocity from the observed line splitting in W49A, we may ask what other information is available from the data relevant to the scaling in core mass and radii in W49A. Although the available observational data do not spatially resolve the individual cores, and we therefore cannot determine their sizes, we may estimate the relative masses of the cores from the observed line intensities integrated over velocity. To the extent that the excitation conditions in the individual W49A cores are similar, the integrated line brightness will be proportional to column density and mass. From the observational data we derive 126, 226, 252, and 282 K km s^{-1} , and a dispersion about the mean of 220 ± 67 or 31%. This dispersion in integrated line brightness in W49A may be compared to the dispersion in core masses, 29% in the hydrodynamic model.

4. CONCLUSIONS

We suggest that:

1. The rotating ring of H II regions, the necklace in W49A, may have formed in the gravitational fragmentation of a molecular cloud flattened by rotation.

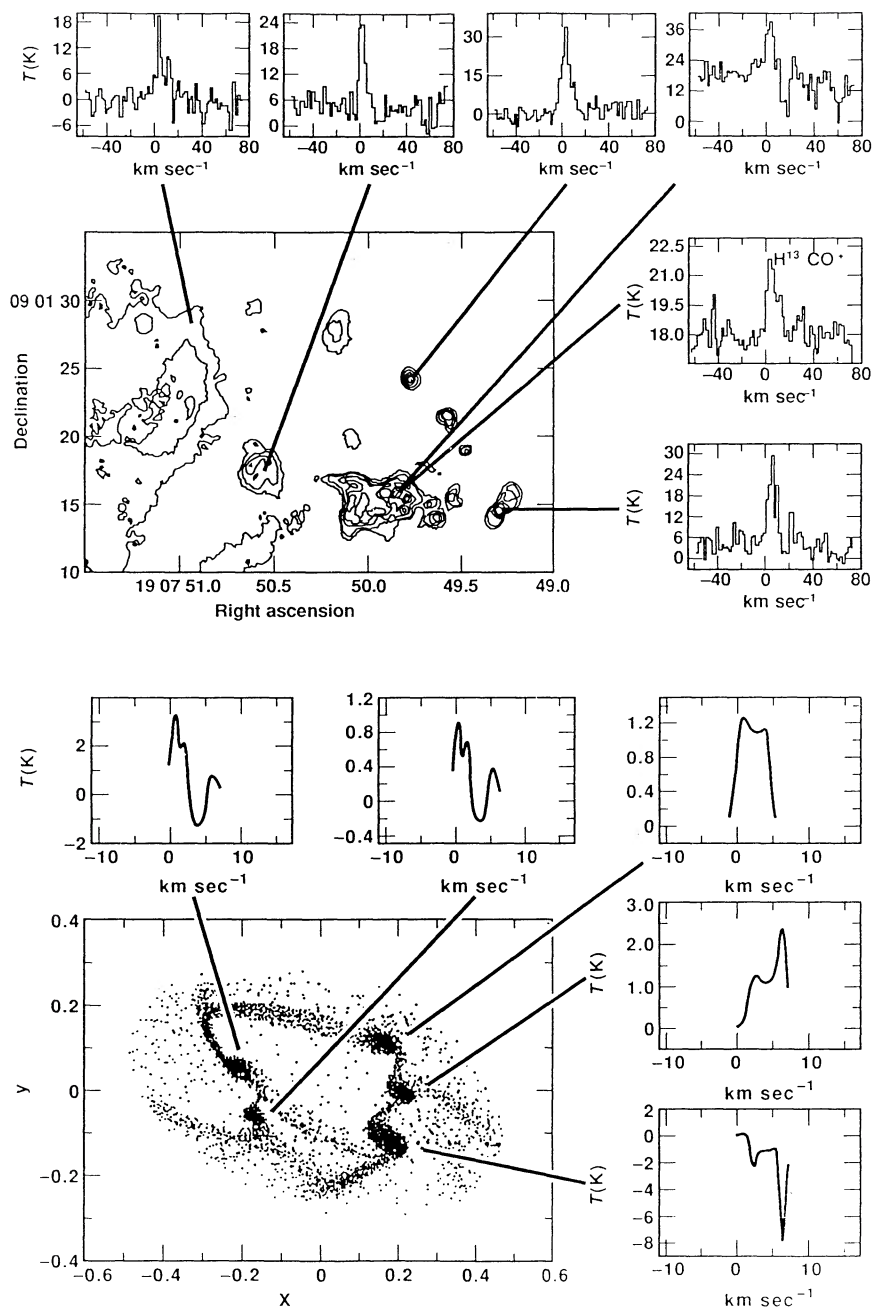


FIG. 4.—Synthetic HCO^+ spectra for our model (*bottom*) and the observations of Welch et al. (1987) (*top*). We have rotated our simulation to a perspective more like that of W49A.

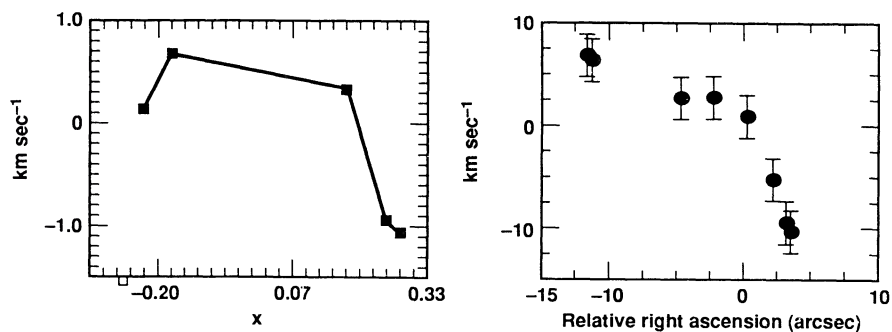


FIG. 5.—Line center velocities of the $\text{H}76\alpha$ recombination line (Welch et al. 1987) (*right*) and line-of-sight radial velocities from our model (*left*).

2. The cloud from which W49A formed had unusually high angular momentum at the time of its initial collapse.
3. The fragmentation process in W49A resulted in a collection of star-forming cores of similar scale in both mass and size.
4. The split emission lines and absorption lines and inverse P Cygni profiles observed in massive star-forming regions are indicative of localized accretion flows in individual star-forming fragments.

Work was performed at the University of Illinois under the auspices of the Laboratory for Astronomical Imaging and at Lawrence Livermore National Laboratory under the auspices of United States Department of Energy under contract number W-7405-ENG-48.

Part of this work has been conducted under the auspices of a special NASA astrophysics theory program that supports a joint Center for Star Formation Studies at NASA-Ames Research Center, University of California at Berkeley, and University of California at Santa Cruz.

REFERENCES

- Dickel, H., & Auer, L. 1991, ApJL, submitted
 Dreher, J. W., Johnston, K. J., Welch, W. J., & Walker, R. C. 1984, ApJ, 283, 632
 Gingold, R. A., & Monaghan, J. J. 1983, MNRAS, 204, 715
 Goldreich, P., & Lynden-Bell, D. 1965a, MNRAS, 130, 97
 ———. 1965b, MNRAS, 130, 125
 Hunter, C. 1964, ApJ, 139, 570
 ———. 1972, Ann. Rev. Fluid Mech., 4, 219
 Keto, E. R. 1990, ApJ, 355, 190
 Keto, E. R., & Lattanzio, J. C. 1989, ApJ, 346, 182
 Larson, R. 1972, MNRAS, 156, 437
 Larson, R. B. 1985, MNRAS, 214, 379
 Layzer, D. 1963, ApJ, 137, 351
 Monaghan, J. J., & Lattanzio, J. C. 1991, ApJ, 375, 177 (ML)
 Rozyczka, M. 1983, A&A, 125, 45
 Rudolph, A., Welch, W. J., Palmer, P., & Dubrulle, B. 1991, ApJ, 363, 528
 Scoville, N., & Kwan, J. 1976, ApJ, 209, 102
 Tohline, J. E. 1980a, ApJ, 235, 866
 ———. 1980b, ApJ, 239, 866
 Welch, W. J., Dreher, J. W., Jackson, J. M., Tereby, S., & Vogel, S. N. 1987, Science, 238, 1550